Upper mantle seismic wave velocity:
Effects of realistic partial melt geometries

William C. Hammond and Eugene D. Humphreys
Department of Geological Sciences, University of Oregon, Eugene

Abstract

We investigate seismic wave velocity reduction resulting from the presence of partial melt in the upper mantle. The amount of shear and bulk modulus reduction produced by the presence of a connected network of realistically shaped and naturally organized melt inclusions is found using finite element calculations. The geometries of the inclusions are taken directly from laboratory experiments of mantle melting, with finite element meshes constructed to conform to these shapes. The shear and bulk moduli of the composite material are found for both the unrelaxed (isolated inclusions) and relaxed (pressure equalized inclusions) cases by assigning appropriate material properties to the fluid. Modulus reduction from deformation simulations of a solid containing realistically shaped and ellipse-shaped melt inclusions quantify the effect of melt pocket cuspateness and melt pocket organization on seismic velocity reduction. The three-dimensional response is estimated from two-dimensional distributions of the melt phase by determining the mode II and mode III components of elastic modulus reduction separately and summing their effects. In general, cuspate and naturally organized melt inclusions cause greater velocity reduction. It is shown that V_P and V_S reduction per percent partial melt are at least 3.6% and 7.9%, respectively. Even higher values for velocity reduction are possible above 1% melt fraction if melt exists only in tubules below 1% melt fraction. The lower, more conservative values of velocity reduction are $\sim$70% greater for V_P and 84% greater for V_S than the analytically determined values for ellipsoidal inclusions. Somewhat greater effects are possible if nonrandom organization of melt occurs on scales greater than our model.

1. Introduction

Measurements of seismic velocity and attenuation are frequently employed to infer the degree and spatial extent of partial melt in the Earth's upper mantle [e.g., *Zhao et al.*, 1992; *Humphreys and Dueker*, 1994; *Sobolev et al.*, 1996; *Xu and Wiens*, 1997; *Dunn and Toomey*, 1997; *Toomey et al.*, 1998]. While tomographic imaging affords the highest resolution of any geophysical technique that images volumes of the deep interior of the Earth [*Forsyth*, 1992], the relationship between the physical state of the mantle and the magnitude of seismic velocity anomalies remains imprecise. Recent studies illustrate just how unconstrained the partial melt content of the upper mantle is (e.g., *Sobolev et al.* [1996], who find that for inferred P wave velocity variations of 3%, the partial melt content can be anywhere between 0 and 3%). Improved understanding of the relationship between mantle physical state and seismic observations has remained problematic because of the contributing effects of various material qualities (e.g., temperature, composition) and to the complexity of the response of realistic partially molten material subject to simple stresses.

The crux of the problem in understanding the effects of partial melt lies in understanding how the microstructural geometry of the pore and conduit shapes containing the melt influences rock elastic properties. Work to date has been focused in two directions: (1) laboratory experimental determination of material properties [e.g., *Sato et al.*, 1988; *Hirth and Kohlstedt*, 1995a, b] and (2) analytic determination of the mechanical response using simplified geometries such as cracks [*O'Connell and Budianski*, 1974], circular and three-grain junction prismatic tubes [*Mavko*, 1980], spheres [*Einstein*, 1906], and ellipsoids [*Eshelby*, 1957; *Wu*, 1966; *Schmeling*, 1985; *Mainprice*, 1997]. Great progress has been made in laboratory determination of the mechanical response to mantle rocks both above [e.g., *Hirth and Kohlstedt*, 1995a, b] and below [*Jackson et al.*, 1992] the solidus. These experiments, however, have not achieved the temperature and pressure conditions that produce partial melting while also deforming the sample on timescales that simulate observed seismic waves.

Analytic results thus far have two limitations. First, the shapes of melt inclusions have been idealized as cracks, spheres, ellipsoids, or simplified cuspate forms which only roughly approximate the true geometries of melt in the upper mantle [e.g., *Waff and*

Bulau, 1979; *Cooper and Kohlstedt*, 1982; *Kohlstedt*, 1992; *Waff and Faul*, 1992; *Faul et al.*, 1994; *Hirth and Kohlstedt*, 1995a]. While it has been argued that the actual shapes can, in terms of summary statistics (such as aspect ratio and form factor), be adequately represented by ellipsoids [*Schmeling*, 1985; *Faul et al.*, 1994], the mechanical response of these shapes systematically differs from simpler geometries with the same aspect ratio. A fluid-filled, convex circular cylinder, for example, is naturally more rigid than a cuspate, concave cylinder with the same melt fraction and aspect ratio [*Mavko*, 1980]. This leads to an underestimation of the amount of velocity reduction for a given partial melt fraction when using relationships based on ellipsoidal geometry. Second, determination of the frequency dependence of the material's elastic modulus and attenuation has been complicated by the need to isolate specific relaxation times (frequencies) associated with the transition between discrete states of stress [*O'Connell and Budianski*, 1977].

Our strategy for determination of the viscoelastic material properties of partially molten peridotite has three parts. It is based on the principle that the dispersion due to anelasticity can be derived from the stress response of the viscoelastic material to a step function in strain. We calculate (1) the elastic response for the "unrelaxed" case in which fluid flow between pores has not yet diminished the differential pore pressure excited by the imposed strain; (2) the elastic response for the "relaxed" case in which pore pressure equilibrium has been attained by fluid flow between pores; and (3) the relaxation time spectrum by estimating the time-scales of interpore flow and pressure equilibrium. Development of the anelastic process and the frequency dependent relaxation, i.e., step 3, is discussed in the companion paper by *Hammond and Humphreys* [this issue], who determine that relaxation occurs sufficiently quickly so that it is the relaxed modulus excited by observed seismic waves. The first two steps use finite element models designed to represent realistic crystal-melt configurations, as inferred from laboratory experiments of partially molten peridotite, as in Figure 1 [*Faul et al.*, 1994].

The advantage of using finite element calculations in the first two steps is that any simple or complex pore shape can be represented with equal ease and elastic interactions between distinct bodies are accounted for. A disadvantage is that certain important intuitions are lost when not treating the problem analytically, so further analysis is required for a detailed
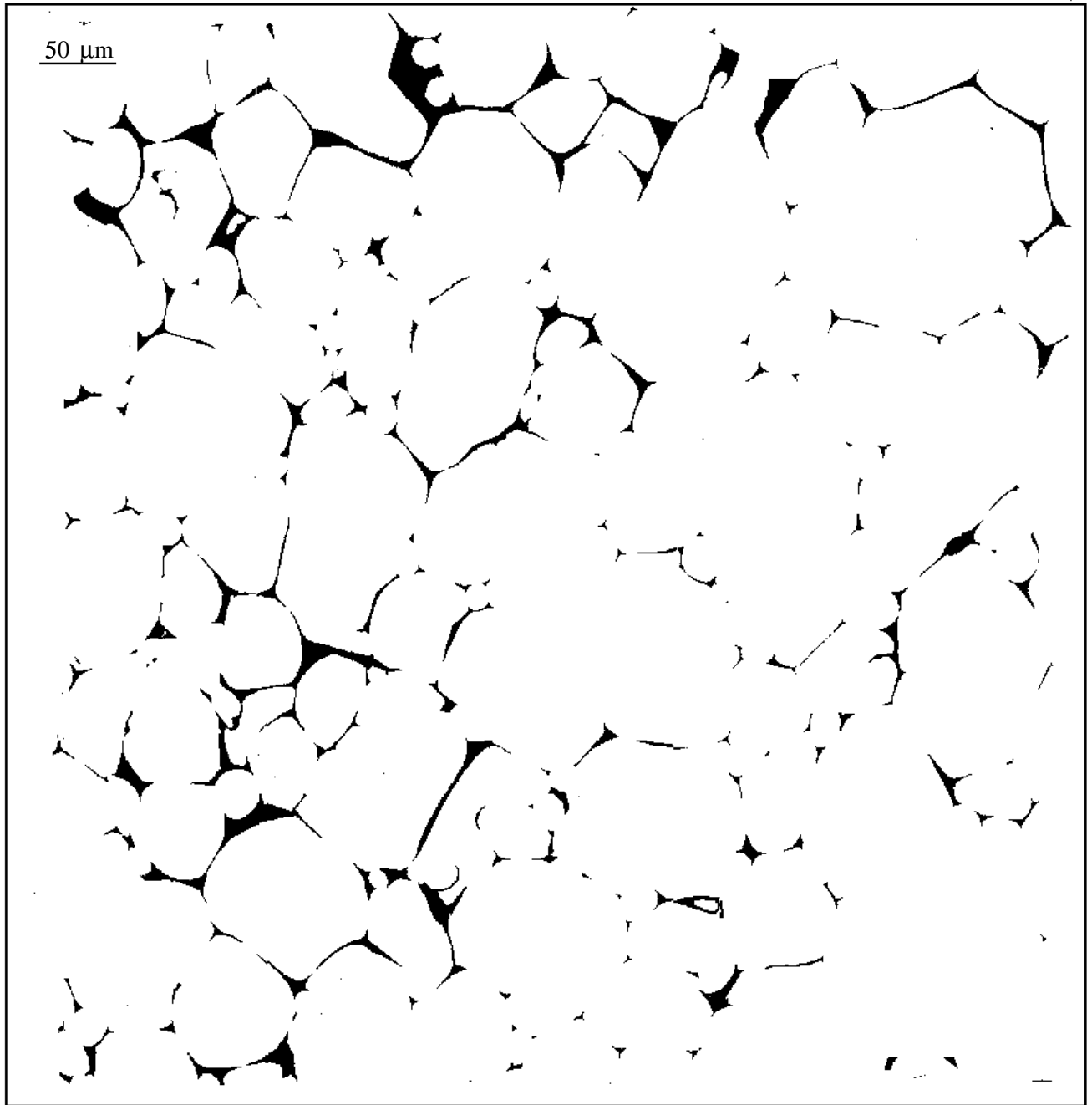
Figure 1

50 μm

Figure 1: Hammond and Humphreys, Jan. 2000

understanding of the underlying processes. In theory, viscoelastic finite elements can be used to evaluate the details of frequency dependence in seismic velocity and attenuation. This is, however, computationally expensive since lower-frequency interactions require unreasonably long run times. A lower bound on the frequencies that can be investigated practically is thus imposed. These two problems are addressed by using an alternative approach, the network representation of *Hammond and Humphreys* [this issue].

Creation of a fully three-dimensional elastic finite element model of realistically shaped and organized melt inclusions is difficult for the following reasons: (1) laboratory mantle melting experimental products from which we derive inclusion shape data are polished flat to expose a single two-dimensional cross section from which we must infer the three-dimensional shape of the melt phase and (2) the crystals that surround the melt are too complex to be meshed by our finite element meshing algorithms. Because of these difficulties we use two finite element analyses that use simpler geometries to approximate the full three-dimensional elastic response to inclusion cuspateness. The first calculation determines the effect of cuspateness and organization on the mode II component of modulus reduction (see Figure 2). The second determines the effect of mode III modulus reduction owing to inclusion cuspateness and organization. The total shear modulus reduction is the sum of the mode II and mode III effects. From the resulting reduced elastic moduli we calculate the amount of V_P and V_S velocity reduction per percent partial melt and compare it to the velocity reduction calculated from ellipse-shaped melt inclusions with the same melt fraction and aspect ratio. The ratio between these two is a seismic velocity "correction factor."

The corrected velocities provide new values for the partial derivatives of seismic velocity with respect to melt fraction. These values can be applied in the interpretation of seismic tomography in the same manner as the derivatives of seismic velocity with respect to temperature, density, and composition.

2. Elastic Effects: Finite Element Calculations

Realistic melt geometries have been determined in laboratory experiments [e.g., *Waff and Bulau*, 1979; *Waff and Faul*, 1992; *Faul et al.*, 1994; *Hirth and Kohlstedt*, 1995a] that simulate mantle conditions to depths of ~70 km. We use images of the melt phase

from *Faul et al.* [1994] (Figure 1) to create finite element representations of the composite material. Details of the experimental configuration and imaging procedures are given by *Faul et al.* [1994] and *Waff and Bulau* [1982]. The melt distribution resulting from these experiments is determined by slicing the run product and by polishing and imaging the glassy inclusions using backscatter electron microscopy. Once the inclusion geometry is in suitable digital format, the shapes are represented in two-dimensional finite elements (Figure 3).

We determine the unrelaxed and relaxed shear moduli with an elastic calculation by using the appropriate elastic constants for elements inside the inclusions. See Table 1 for specific values. To simulate the unrelaxed case, the shear modulus of the melt is assigned a value that is essentially zero, while its bulk modulus is approximately that of a basaltic liquid. The response thus represents times after shear stresses in the fluid have relaxed but hydrostatic stresses remain. When the external strain is imposed, the pressure inside each inclusion, which is a function of its shape and orientation, is calculated by the finite element algorithm.

For the relaxed case we assume that all inclusions are interconnected and that fluid flow has occurred, equalizing the inclusion pressures. Since the differences in pressure between inclusions are identically zero and since the average hydrostatic stress throughout the solid due to macroscopic shear strain is zero, we can simulate this stress state by assigning shear and bulk elastic moduli to essentially zero inside the inclusions, effectively filling the inclusions with vacuum [*Mavko*, 1980]. This technique is appropriate for modeling shear stress relaxation from melt squirt but not for bulk relaxation. It is argued by *Hammond and Humphreys* [this issue], however, that bulk effects are probably negligible compared to shear effects. Thus we model the effects of melt squirt arising only from imposed shear.

The finite element calculations determine the displacements to all nodal positions that minimize the global elastic strain energy. Stresses and strains are calculated everywhere with element shape functions and elastic constitutive relations subject to the displacements applied as boundary conditions. Figure 4 is a close up view of the hydrostatic strains near a three-grain junction resulting from a macroscopically applied shear displacement boundary condition. For the two-dimensional results presented here, isoparametric triangular quadratic elements with isotropic
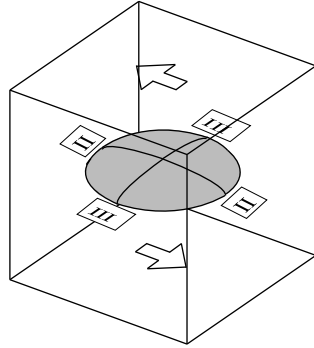
Three-dimensional
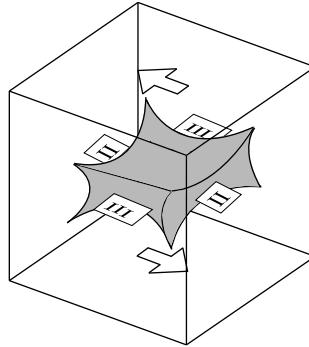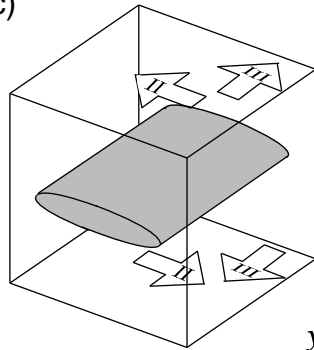
a)

b)

Two-dimensional

c)

d)

(a)

(b)

Maximum Dilation   0   Maximum Compression
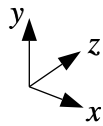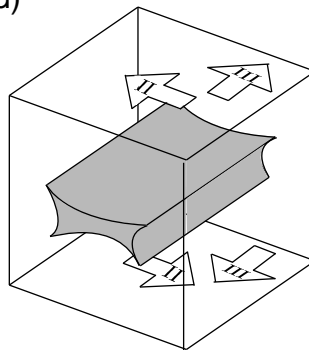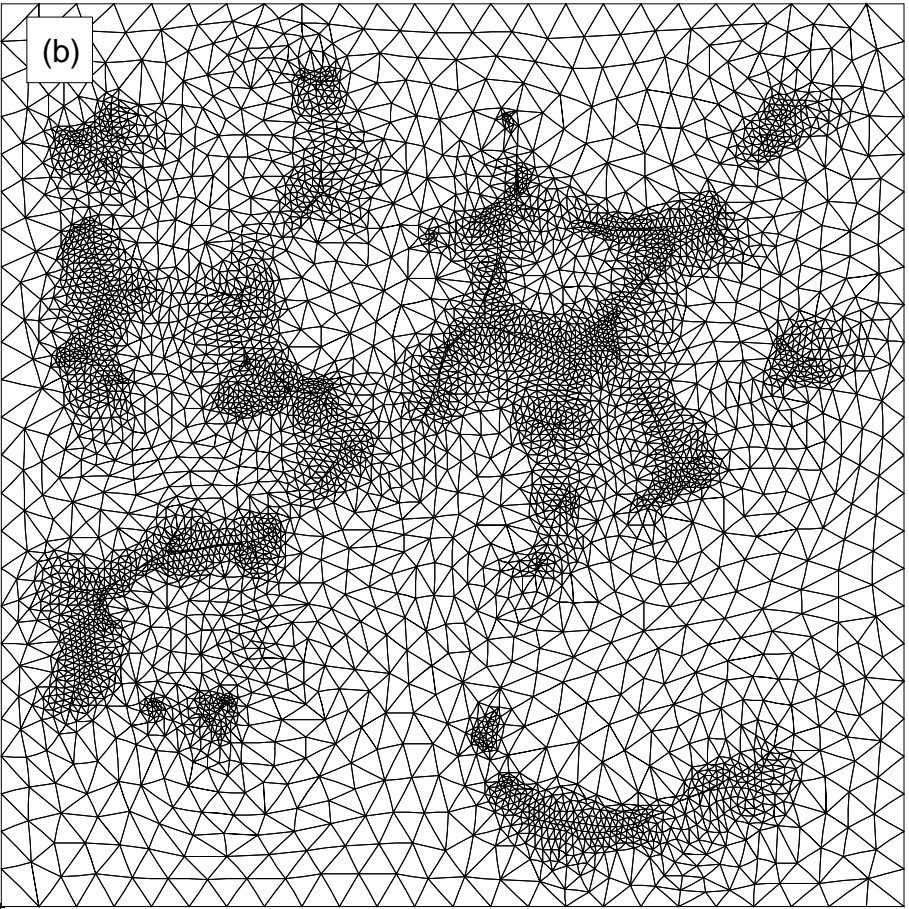
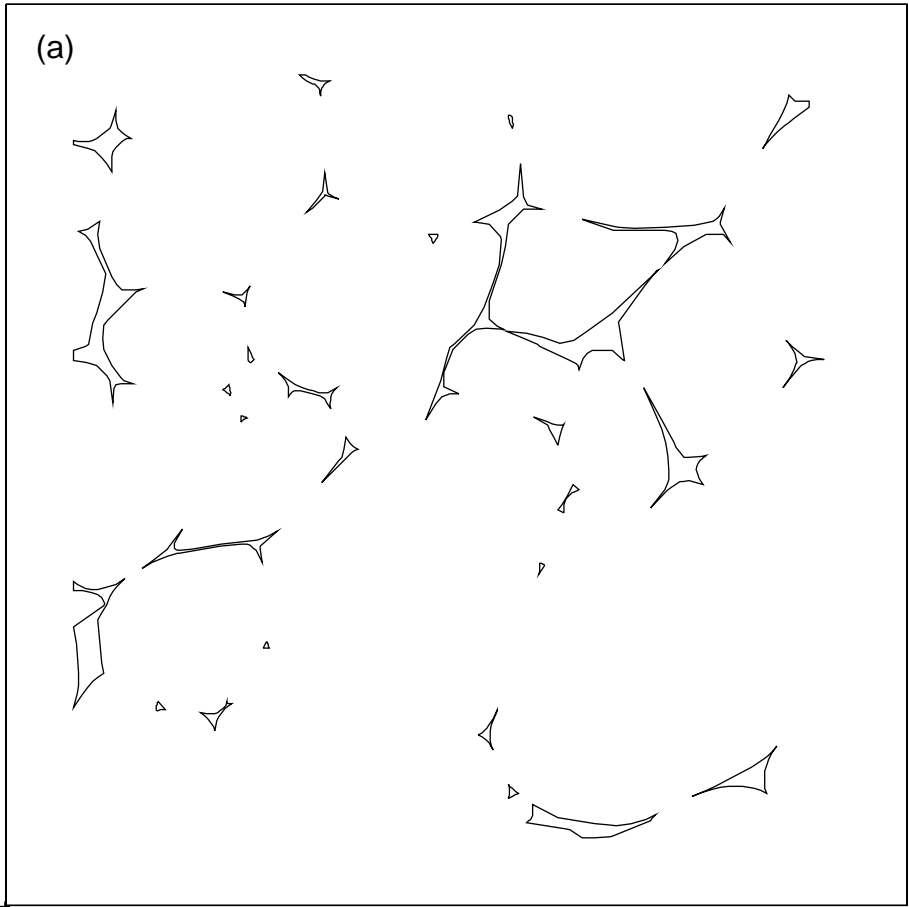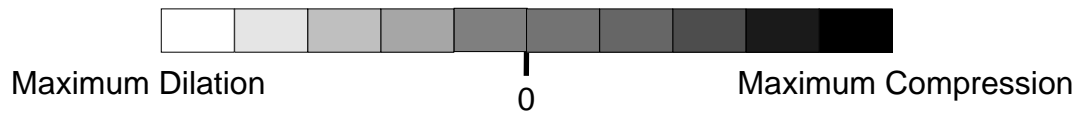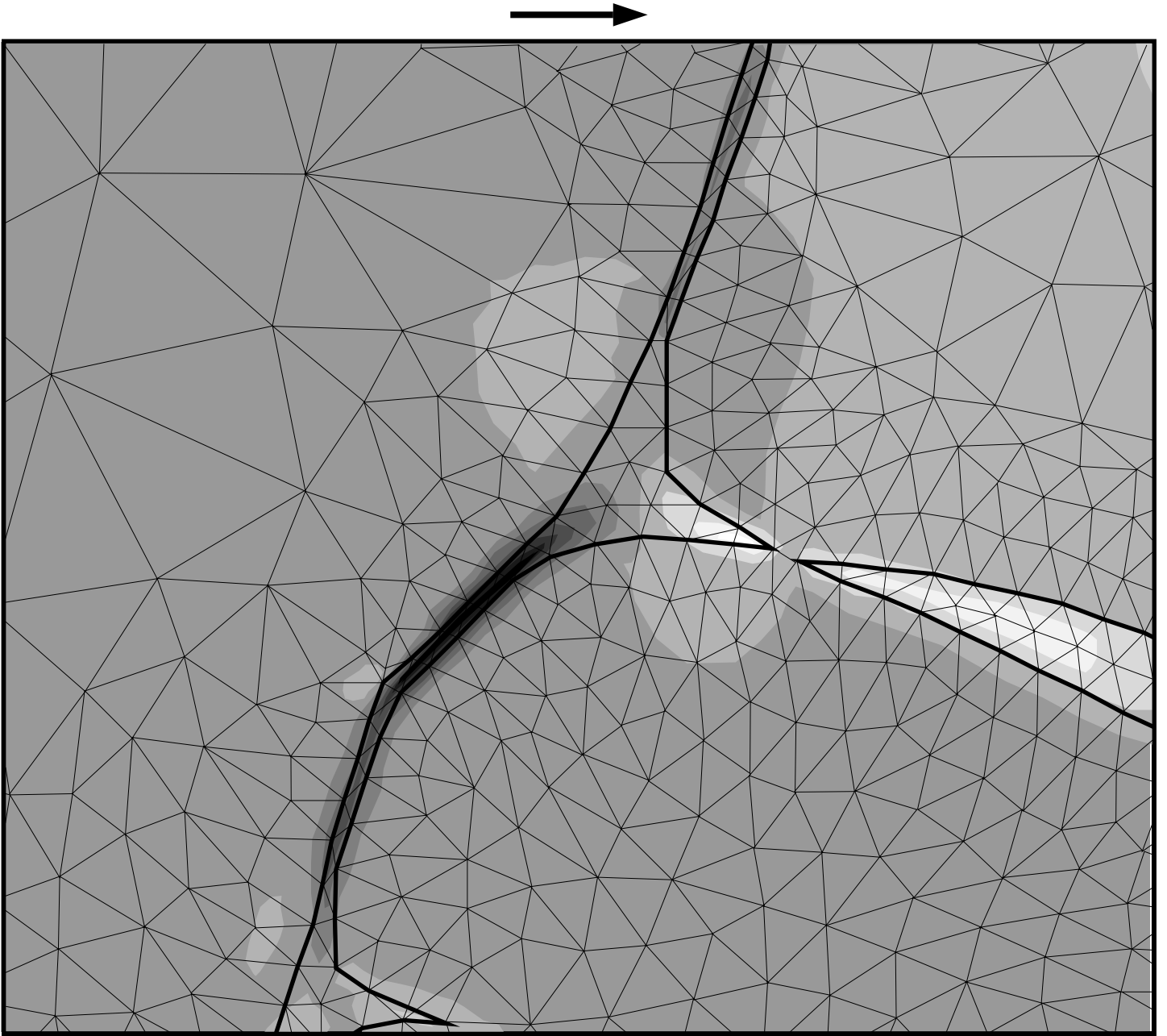solid elasticity were used, while for the three-dimensional calculations isoparametric wedge-shaped linear elements were used [e.g., *Zienkiewicz and Taylor*, 1989]. Mesh generation is accomplished through a semiautomatic routine. All the finite element calculations presented here were performed with the commercial software package MSC PATRAN/Advanced FEA, a product of the MacNeal Schwendler Corporation.

2.1. Numerical Accuracy

To verify that our finite element modeling provides accurate results, two tests were performed. First, the nodal density was progressively increased until displacements and stresses did not change significantly even around the complicated cuspate inclusion tips and in areas of inclusion interaction. Second, a relatively complex case for which an analytic solution exists was tested. *Mavko* [1980] solved for the amount of elastic modulus reduction due to the presence of a cuspate cylindrical pore of "triple junction" cross section shape. For a single dry pore (i.e., an inclusion with no fluid inside) with shape parameter $\epsilon = 0$ (the most cuspate possible), length d, radius R, solid shear modulus μ_s, Poisson's ratio ν_s, bulk modulus K_s, and total volume V, the bulk modulus of the composite K_d is given (after correction for a minor error from Appendix A of *Mavko* [1980]) by

$$\frac{1}{K_d} = \frac{1}{K_s} + \frac{\pi R^2 d}{4\mu_s V}(1 - 2\nu_s)[12 + \frac{1 - 2\nu_s}{1 + \nu_s}]. \quad (1)$$

Using $\nu_s = 0.25$, $K_s = 46.67$ GPa, $\mu_s = 28.0$ GPa, $R = 1$, $V = 1000$ (the solid is a $10 \times 10 \times 10$ cube), and $d = 3$ yields $K_d = 45.56$ GPa.

A dry cuspate tubule of identical dimensions has been encased in a finite element solid and compressed with hydrostatic displacement boundary conditions (Figure 5). Our calculation differs from that of *Mavko* [1980] in that we use finite elements, rather than an analytical method. Thus we took care to minimize the effects of the boundary by making the volume large enough so that stresses are close to uniform across each face of the cube, yet small enough so that the pore introduces sufficient weakness to the composite. The stresses measured on the surfaces are averaged over each face.

The effective bulk modulus calculated from finite elements is the simple ratio of calculated hydrostatic stress to imposed strain, $K_d = 45.567$ GPa, an error of <0.03% in calculation of the composite elastic modulus, and an error of <1% in calculation of the drop in modulus. This level of error is acceptable

given the magnitude of differences found between the moduli of solids with ellipse shaped and realistically shaped inclusions, as discussed below.

2.2. Shear Modulus

Our goal is to calculate the reduction in shear modulus owing to porosity in a three-dimensional solid. The material contains complicated melt inclusions that vary in all three dimensions, making direct computation of the modulus with the finite element method beyond our reach. We therefore assume that the elasticity resulting from the true melt geometries can be approximated by that of three-dimensional biaxial ellipsoids of *Schmeling* [1985] and then compute perturbations to this result for the effects of inclusion cuspateness and organization.

To determine the elastic shear modulus with finite elements, boundary conditions are applied that drive macroscopic simple shear strain on the finite element mesh. In Figure 3b, for example, the top of the mesh is translated parallel to the bottom boundary, which is held fixed. Imposing a left-to-right wrap around boundary condition makes the sample effectively infinite and periodic in the horizontal dimension, ensuring that macroscopic simple shear is enforced. The finite element calculation provides the stress associated with the macroscopic strain, so the elastic shear modulus of the composite material is obtained by

$$\sigma_{ij} = \lambda\varepsilon_{kk}\delta_{ij} + 2\mu\varepsilon_{ij}, \quad (2)$$

where δ_{ij} is the Kronecker delta function, λ is Lamé's first constant, and μ is the shear modulus. When $i \neq j$, σ_{ij} is the shear stress related solely to shear strain ε_{ij}.

The effect of melt inclusion cuspateness on elastic shear modulus reduction has two modes as illustrated by the tags II and III in Figures 2a and 2b. The volume in Figure 2b is weaker than the volume in Figure 2a because of the sum of the effects of cuspateness in mode II and mode III. Cuspateness on the front and back of the inclusion (with respect to the direction of the applied shear, i.e., the x direction) affects the mode II component of modulus reduction. Cuspateness to the sides of the inclusion (normal to the shear direction, i.e., along the z direction) affects the mode III component of modulus reduction. Because of limitations in our ability to model complex melt geometries in three dimensions with finite elements, we cannot directly calculate the simultaneous effects of mode II and mode III cuspateness. We can express
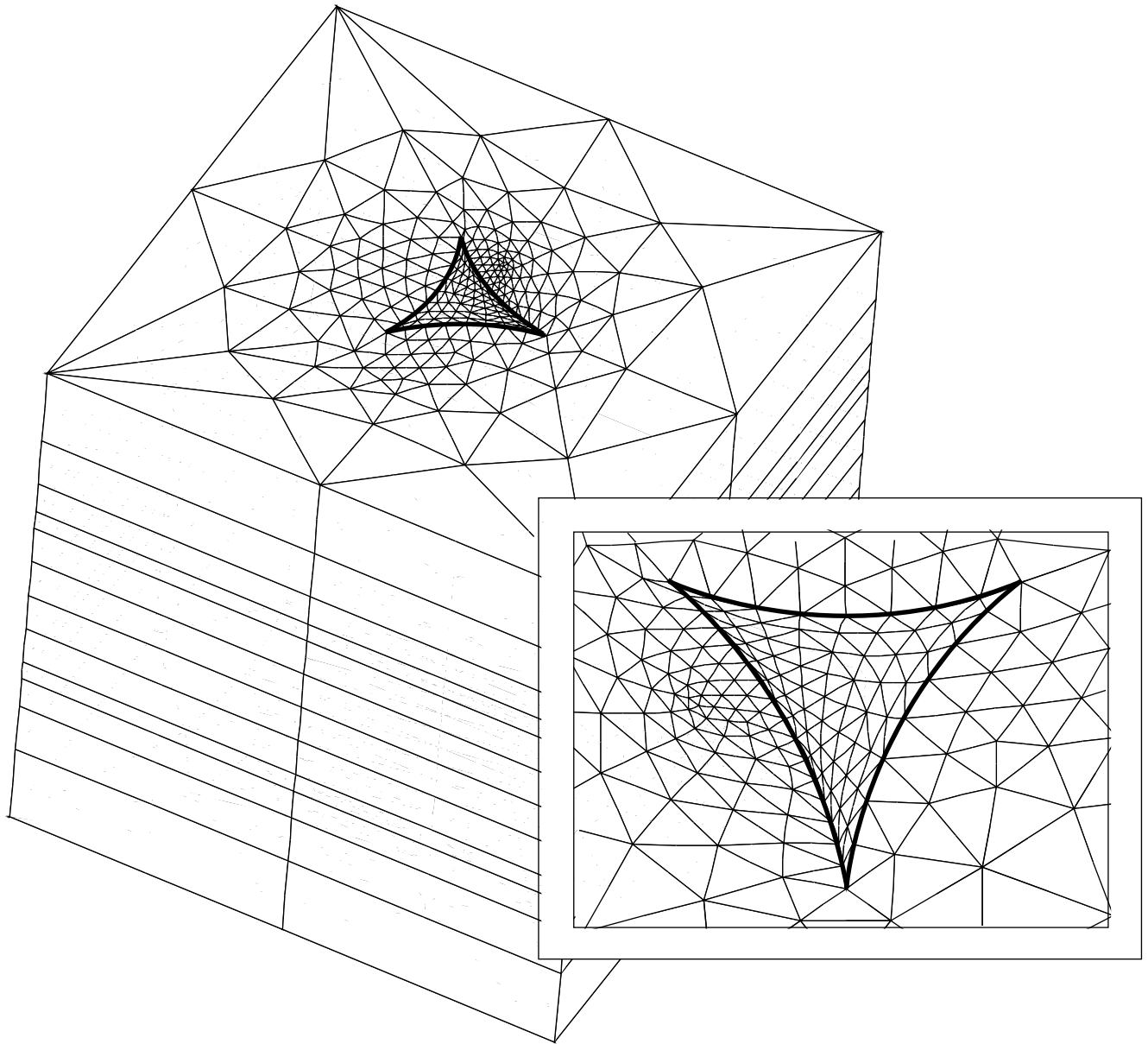
the effect of cuspateness in the two orthogonal directions as a function of generalized mode II and mode III shape parameters ϵ_{II} and ϵ_{III}

$$\mu_{\text{cuspate}} = f(\epsilon_{II}, \epsilon_{III}). \qquad (3)$$

This function may not be linear with respect to ϵ_{II} and ϵ_{III}, but because the changes in modulus are small, we assume a local linearity and express the modulus reduction as the sum of two corrections, one for each mode:

$$\mu_{\text{cuspate}} \approx \mu_{\text{ellipsoid}} + \Delta\mu_{II} + \Delta\mu_{III}, \qquad (4)$$

where $\mu_{\text{ellipsoid}}$ is the modulus calculated for randomly oriented ellipsoids [*Schmeling*, 1985].

We determine the total drop in shear modulus from the ellipsoidal case to the cuspate inclusion case by performing separate tests in shear mode II and mode III, as represented in Figures 2c and 2d. The finite element mesh shown in Figure 3 addresses mode II modulus reduction, since the two-dimensional mesh is equivalent to providing xy shear to the blocks in Figures 2c and 2d. The drop in mode II shear modulus is calculated by comparing results using the mesh in Figure 3b and a similar mesh with ellipse-shaped inclusions of the same average aspect ratio and melt fraction. The shear moduli for each are calculated using (2) and the difference in moduli provides the mode II shear modulus correction $\Delta\mu_{II}$ in (4).

The mode III modulus correction $\Delta\mu_{III}$ is determined using a three-dimensional mesh created by projecting the mesh in Figure 3b into the plane of the figure (the "z" dimension). This results in a mesh composed of wedge-shaped elements, triangular on two faces and rectangular on three faces. The yz shear modulus (mode III) is obtained by displacing the top face in the z direction while holding the bottom face fixed. The xz modulus is determined analogously. In this simulation the x and y degrees of freedom are removed, eliminating the need for a wrap around boundary condition. Material properties are the same as those used in the two-dimensional mesh.

Calculations based on the finite element mesh in Figure 3 reveal that our sample exhibits significant elastic anisotropy. It has an elastic shear modulus that varies with orientation of the applied shear by about $\sim$2.6% for the unrelaxed and 3.5% for the relaxed cases per percent partial melt. The effects of elastic anisotropy in the sample were removed by subjecting the sample to separate simulations in pure and simple shear. The shear modulus in a two-dimensional anisotropic medium has a $\cos(4\theta)$ dependence, where θ is the orientation of the sample with respect to the applied shear. Thus we found the directionally averaged shear modulus by averaging the moduli determined at two orientations differing by $\pi/4$. Testing the sample in both pure and simple shear is equivalent to rotating the sense of shear by $\pi/4$, so averaging these results provides the directionally averaged shear modulus. Isotropic shear moduli for the model in Figure 3, and for a similar model with ellipsoidal inclusions of the same melt fraction and aspect ratio, are used to calculate the correction factor for inclusion cuspateness.

Natural partially molten rocks differ from randomly oriented ellipsoids in an additional way. While analytic solutions for the effect of melt on seismic velocities represent the liquid phase as inclusions that are randomly oriented and distributed [e.g., *Mavko*, 1980; *Schmeling*, 1985], real melt pockets form on the faces of crystalline grains and adjacent to triple junction tubules, thus tending to meet end to end and in nonrandom fashion (e.g., see Figure 1). Thus a correction factor for inclusion organization is also determined. The effect of inclusion organization on elastic shear modulus reduction is measured by randomizing inclusion location and orientation in the model space and comparing the modulus reduction effect of these randomly distributed inclusions with that caused by the naturally organized inclusions. Iteratively repeated randomizations and finite element analyses were performed until it was clear that the average for the moduli were stable with respect to permutations of inclusion location and orientation. Care was taken to select random samples that exhibit smaller degrees of elastic anisotropy. Five reorganizations were performed providing mean shear moduli presented in Table 2 under "random cuspate" films. The standard error estimates for the mean modulus are approximately $\sim$0.5% of their mean values. This error is over an order of magnitude less than the difference in modulus between tubules and ellipsoids and one sixth the difference between relaxed cuspate and organized films. Thus we have obtained the directionally averaged shear modulus to within required tolerance. For P and S waves the effect of inclusion cuspateness is between 1.1 and 5 times greater than the effect of inclusion organization, depending on whether the melt is relaxed or unrelaxed, respectively.

In Table 2 the effect of the various corrections are shown in terms of the percent seismic velocity reduc-

Table 2

tion per percent partial melt $\partial \ln V / \partial F$. Our correction factors are applied to the velocity reductions determined by the analysis of three-dimensional randomly oriented ellipsoidal pores of *Schmeling* [1985]. These derivatives are functions of melt fraction, as described in section 3. They are estimated by

$$\frac{\partial \ln V_P}{\partial F} \approx \frac{\ln V_{P2} - \ln V_{P1}}{F_2 - F_1}, \qquad (5)$$

$$\frac{\partial \ln V_S}{\partial F} \approx \frac{\ln V_{S2} - \ln V_{S1}}{F_2 - F_1}, \qquad (6)$$

$$\frac{\partial \ln V_P}{\partial \ln V_S} = \frac{\partial \ln V_P / \partial F}{\partial \ln V_S / \partial F}, \qquad (7)$$

where V_{Pi} is the P wave velocity and V_{Si} is the S wave velocity at melt fraction F_i. We assume that the effect of the presence of melt on the density of the rock with respect to seismic velocity is small enough to be ignored and that velocity reduction is linear with melt fraction. The melt fraction F of the sample shown in Figure 3 is 2.0%.

2.3. Bulk Modulus

Bulk modulus, compared to shear, is relatively insensitive to inclusion orientation. Thus a single experiment was performed in which inclusions of realistic geometries were compared to a sample with the same porosity having ellipse-shaped inclusions of the same average aspect ratio. To excite the bulk modulus, the boundary conditions on the finite element sample are changed so that all four boundaries of the solid are displaced toward the center of the sample. We find that the bulk modulus is relatively insensitive to the differences in inclusions shape (i.e., cuspate versus ellipsoidal) analyzed here. Furthermore, the difference between the relaxed and the unrelaxed bulk modulus is negligible since variations in hydrostatic pressure between inclusions are relatively small as a result of macroscopically applied bulk compression, and hence little fluid flow occurs. Thus, for the remainder of this analysis, perturbations in seismic velocity due to inclusion shape are assumed to take place via the the shear modulus alone, leaving the bulk modulus constant. For the calculations we use $K = 45.72$ GPa, the value predicted by *Schmeling* [1985] for randomly oriented ellipsoids with aspect ratio $\alpha = 0.05$ and melt fraction $F = .02$.

3. Discussion

Our goal has been to better understand the effect of partial melt on seismic wave propagation in the upper mantle. Among the conditions that influence seismic wave propagation, the effects of partial melt are relatively poorly understood, primarily because the specifics of the melt geometry are important in addition to the quantity of melt. We have thus concentrated our efforts on obtaining a refined estimate of elastic modulus reduction of upper mantle rocks containing small amounts of melt in realistic geometries, as inferred from laboratory experiments of upper mantle partial melt.

With utility for seismologists in mind, we devise a simple scheme for estimating partial melt content and perturbations in temperature based on resolved seismic wave velocity reduction. The presumption is that the sensitivity of seismic velocity to the presence of melt is provided by the derivatives $\partial \ln V_P / \partial F$, $\partial \ln V_S / \partial F$ (for partial melt), and $\partial \ln V_P / \partial T$, $\partial \ln V_S / \partial T$ (for temperature variations). These derivatives are quantities that have been, in part, determined in section 2 (for partial melt, see Table 2) and by laboratory studies of the elastic and anelastic properties of single crystal olivine and peridotitic rocks [e.g., *Karato*, 1993; *Isaak*, 1992; *Jackson et al.*, 1992].

3.1. Effect of Melt Fraction

Laboratory experiments suggest that as melting proceeds, the first liquid is contained predominantly in long, narrow triple junction tubules. As melt content increases, a greater proportion of the melt resides in film-like pores. This is supported by laboratory studies of the effect of temperature on seismic velocity, which show that as the solidus is crossed, a gradual transition from subsolidus to supersolidus rate of velocity change occurs [*Sato et al.*, 1988]. This experiment also showed that as melt fraction increased, seismic velocity reduction per percent partial melt increased until becoming approximately constant (in their study at around 5% melt fraction). Additionally, high-pressure experiments designed to explore the geometries of partial melts produce, at melt fractions <2%, nearly all melt contained in triple junction tubules [*Waff and Bulau*, 1979]. *Faul et al.* [1994] specifically address the distinction between oblate-versus prolate-shaped inclusions and find that dominance of the disk-shaped inclusions extends to melt fractions as low as 0.75%. Above this threshold $\sim$80% of the melt is sequestered in disk-shaped inclusions. A consistent explanation for these observations is that as the solidus is crossed, the first melt appears as triple junction tubules, then as the temperature in-

creases, further films appear and grow to dominate [*Waff and Faul*, 1992]. We define these two domains by specifying the temperature T_{film} above which the film geometry dominates. We select the T_{film} that corresponds to $F = 1\%$, a value most consistent with that of *Faul et al.* [1994], since this study addresses this question most directly. In section 3.2 we take this behavioral transition into account by considering two paradigms for the style of evolution in partial melt containment as melt fraction increases. Partial derivatives of seismic velocity with respect to melt fraction corresponding to each paradigm are presented in Table 2. The first paradigm assumes that partial melt is predominantly contained in cuspate penny shaped inclusions (Figure 3) whose aspect ratios are constant with melt fraction. The ratio of melt contained in tubules versus film-like pores remains fixed for all melt fractions. The second paradigm allows for the first melt to appear as triple junction tubules, transitioning into a film dominated regime with increasing melt fraction. In this case separate representations are used for the very low melt fraction regime (tubules) and for the higher melt fraction (file-like shapes) dominated regime. We use the partial derivatives calculated by *Mavko* [1980] for triple junction tubule shape pores below T_{film}. Above T_{film} we use the derivatives for cuspate organized inclusions satisfying our calculated velocity reduction at 2% melt fraction. Above T_{film} the velocity reduction derivatives are greater than for the case where the melt is contained in films for all melt fractions since V_{P1} and V_{S1} are due to the effect of tubules at T_{film}.

3.2. Determining Seismic Velocity Reduction From Temperature and Melt Fraction

Determining temperature perturbation and partial melt content from V_P and V_S reductions is an inverse process that relies on a sound forward calculation using known effects of partial melt and temperature. Anelastic (attenuating and frequency dependent) as well as anharmonic (frequency-independent and nonattenuating) effects must be considered above and below the solidus. When observations of Q are available, estimates for the velocity reduction due to solid state anelasticity can be obtained using relationship (6) of *Karato* [1993]. In this case a velocity perturbation from the background can be translated directly to values for amount of temperature change and quantity of partial melt. In general, we can semilinearize the temperature and melt fraction dependence of V_P as

$$\frac{\Delta V_P}{V_P} = \left[\frac{\partial \ln V_P}{\partial T}_{ah} + \frac{\partial \ln V_P}{\partial T}_{ae} \right] \Delta T, \quad (8a)$$

when $T < T_s$;

$$\frac{\Delta V_P}{V_P} = \left[\frac{\partial \ln V_P}{\partial T}_{ah} + \frac{\partial \ln V_P}{\partial T}_{ae} \right] \Delta T + \left(\frac{\partial \ln V_P}{\partial F}_{\text{tube}} \right) F, \quad (8b)$$

when $T_s < T < T_{\text{film}}$; and

$$\frac{\Delta V_P}{V_P} = \left[\frac{\partial \ln V_P}{\partial T}_{ah} + \frac{\partial \ln V_P}{\partial T}_{ae} \right] \Delta T + \left(\frac{\partial \ln V_P}{\partial F}_{\text{tube}} \right) F_{\text{film}} + \left(\frac{\partial \ln V_P}{\partial F}_{\text{film}} \right) (F - F_{\text{film}}), \quad (8c)$$

when $T_{\text{film}} < T$. In each case $\Delta T = T - T_0$ and T, T_0, and T_s are temperature, temperature of nonanomalous mantle, and solidus temperature (°C) respectively. F is melt fraction which is a function of temperature. F_{film} is the melt fraction above which films become the dominant form of melt containment, occurring at temperature T_{film}. The *ae* and *ah* subscripts denote the anelastic and anharmonic derivatives, respectively. This relationship has an exact analog for S waves, which is not written here. The first paradigm for melt containment can be represented by letting $T_{\text{film}} \rightarrow T_s$, which effectively eliminates (8b).
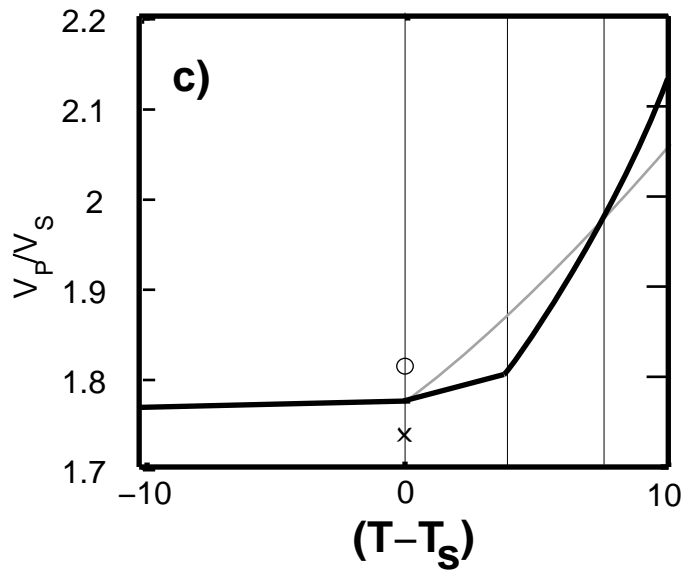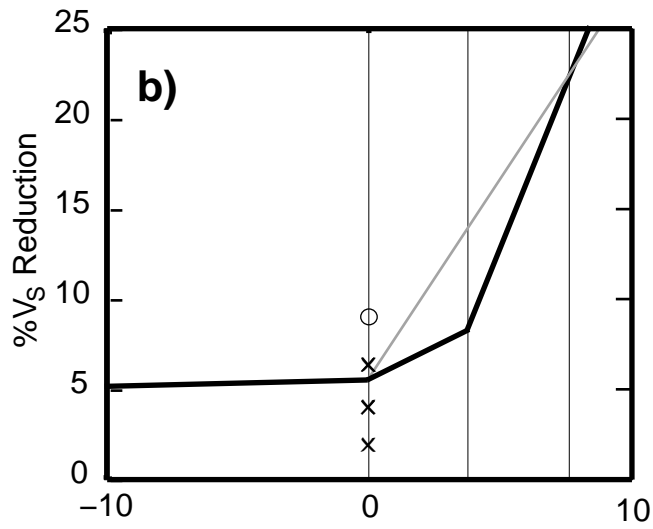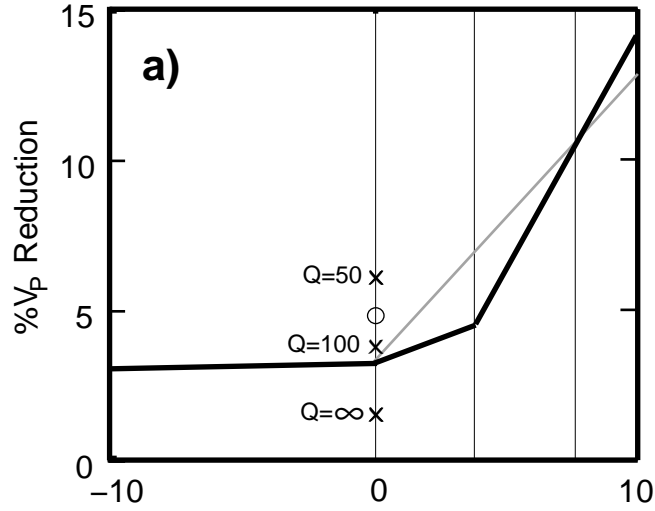
Equation (8) is only semilinearized because of the dependence of the partial derivatives on temperature. The values of the derivatives in the first two terms are given by *Karato* [1993], while the derivatives of the two right-hand terms can be found in the relaxed column of Table 2 for organized cuspate films. Evidence that the relaxed modulus is appropriate is provided by *Hammond and Humphreys* [this issue]. We can use the temperature dependence of F to eliminate F and write (8) solely as a function of temperature. We use

$$F = -17.16 + 0.025(T) - 9 \times 10^{-6}(T^2) \quad (9)$$

found by *Baker and Stolper* [1994] for the melting of peridotite. In this relation, $1240 \leq T < 1340°C$ at 10 kbar, appropriate for dry mantle. Addition of water to the system will depress T_s considerably.

Figure 6 shows the amount of cumulative seismic velocity reduction for P and S waves as a function

Figure 6

F= 0% 1% 2%

a)

%V_P Reduction

Q=50 ✕
Q=100 ✕
Q=∞ ✕

−10   0   10

b)

%V_S Reduction

−10   0   10

c)

V_P/V_S

$(T-T_S)$

of temperature. The crosses indicate velocity reduction at the solidus for reference $Q = 50$, $Q = 100$, and $Q = \infty$, assuming Q is held constant. The lines indicate velocity reduction as a function of temperature and melt fraction with Q that varies with temperature, as discussed below. The slope of the lines below T_s are the sums of the temperature and Q-dependent derivatives for the effects of anelasticity and anharmonicity for solid state mantle. Using the relations of *Karato* [1993], we have activation enthalpy $H^* = 500$ kJ/mol and the frequency dependence of Q parameter $F(\alpha) = 1$ to determine the derivatives for these ranges of T and Q. Anharmonic derivatives are $d\ln V_{P0}/dT = -0.62 \times 10^{-4}$, $d\ln V_{S0}/dT = -0.76 \times 10^{-4}$ and are constant over the temperature ranges studied here [*Isaak*, 1992]. The resulting cumulative velocity reduction for each temperature comes from integrating the derivatives numerically:

$$\frac{\Delta V}{V} = \int_{T_0}^{T} \frac{1}{V(T)} \frac{dV}{dT} dT. \tag{10}$$

Above T_s, $d\ln V/dT$ is the sum of the effect of temperature on the solid matrix and the effects of partial melt derived earlier. We assume that at small melt fractions, melt-induced effects are additive to solid state effects and that the presence of melt is not concentrating strain at grain boundaries thereby reducing the contribution of solid state effects. Thus at each temperature above the solidus and below T_{film}, we add the additional velocity perturbation

$$(\frac{d\ln V}{dF})_{\text{tube}} F, \tag{11}$$

while above T_{film} we add

$$(\frac{d\ln V}{dF})_{\text{tube}} F_{\text{tube}} + (\frac{d\ln V}{dF})_{\text{film}}(F - F_{\text{tube}}) \tag{12}$$

at the appropriate temperature determined by (9). These relationships can be calculated for every depth interval of interest, providing velocity perturbations from melt content and temperature.

The effect of temperature on solid state Q_S in upper mantle rocks has been studied in the laboratory by *Jackson et al.* [1992], who showed that Q_S has a roughly exponential dependence on temperature between 600 and 1000°C. Their results can be approximately summarized by

$$Q_S(T) = 1.6 \times 10^3 e^{-3.466 \times 10^3 T}. \tag{13}$$

The effect of the temperature dependence of Q on the total percent seismic velocity reduction is shown with the heavy solid lines in Figure 6. While actual separate measurements for Q_S and Q_P would be preferable, this is not always practical. Since bulk attenuation in the mantle is negligible, Q_P can be estimated from Q_S by [*Anderson*, 1989]

$$Q_P = \frac{3}{4}(\frac{V_P}{V_S})^2 Q_S. \tag{14}$$

The solid lines in Figure 6 show examples of the effect that Q dependence has on velocity reduction.

The ratio between P and S seismic wave velocity is shown in Figure 6c as a function of temperature. The values are calculated as the simple ratio between V_P and V_S velocity assuming that at the nonanomalous mantle temperature $V_P/V_S = \sqrt{3}$. Melt has the dominant effect on V_P/V_S. Above T_s, perturbations in V_P/V_S increase with increasing melt fraction, e.g., $V_P/V_S \approx 2$ at $F = 2\%$.

3.3. Determining Temperature and Melt Fraction from Seismic Velocity Reduction

Seismology offers a direct means for inferring the presence of partial melt in the upper mantle. Inverting seismic velocity to determine the temperature and melt content has two sources of uncertainty: (1) imperfect resolution leading to underestimates in the amplitude of seismic velocity anomalies and (2) the less than ideal understanding of the relationships between velocity reduction and the physical parameters causing velocity reduction. With uncertainty in the relationship between melt fraction and velocity reduction aside, other issues relating velocity and physical state still remain a concern. For example, the relationship between temperature and melt fraction, the temperature dependence of Q, and values for H^* are not known with great certainty. Some of these are pressure-dependent and thus need to be tailored to the specific depth intervals of interest.

3.4. Anisotropic Conditions

Experimental studies of partially molten mantle materials indicate that penny shaped melt pores become preferentially aligned in the presence of nonhydrostatic stress conditions [*Jin et al.*, 1994; *Kohlstedt and Zimmerman*, 1996; *Bai et al.*, 1997; *Daines and Kohlstedt*, 1997; *Karato et al.*, 1998; *Zimmerman et al.*, 1999]. Preferred orientation of melt pockets in the mantle will cause anisotropy of seismic wave velocity

and attenuation, and anisotropic melt distributions will tend to cause further elastic shear modulus reduction as additional end-to-end alignments of melt inclusions are created. An estimation of the effects of this type of organization requires a continuation of our study and is not the subject of this paper. Our conclusions on elastic modulus reduction may be viewed as lower-bound estimates of the effects of melt inclusions when significant inclusion anisotropy is present.

The conclusion that use of the relaxed modulus is appropriate for upper mantle studies in the seismic band is still valid in the presence of preferential melt inclusion alignment. This is because preferential alignment does not result in an increase of attenuation in the seismic band [*Hammond and Humphreys, this issue*].

3.5. Scale of Inhomogeneity

Most experiments that explore the geometries of interstitial melt pockets are performed on samples of synthetic peridotite-like materials that are created in the laboratory. Chemical and grain size heterogeneity are carefully controlled in order to construct simple but representative models of natural rock.

Natural samples of peridotite possess inhomogeneities on greater scales than the $\sim$1mm capsule size of laboratory analyses. A quick look at the top quarter of Figure 1 shows that even within laboratory samples, melt organizes itself into structures that create larger zones of weakness within the material. We see from section 2.2 and Table 2 that the effect of organizing inclusions into nonrandom arrangements that elastically interact with one another is to further reduce the shear modulus. Thus any larger-scale organizations or deviations from idealizations of melt geometries will always serve to reduce seismic velocities further. Although this effect is most likely small in the upper mantle, it is added to the fact that we apply a two-dimensional cuspateness correction factor to three-dimensional ellipsoids, which also tends to underestimate the velocity reduction. The values in Table 2 thus represent minimums for the derivatives of velocity with respect to melt fraction.

4. Conclusions

We have estimated the effect of upper mantle partial melt on seismic P and S wave velocities. Our contribution to this effort has been to estimate two correction factors to the commonly used randomly ori-

ented ellipsoidal melt inclusion model. These include a correction for melt inclusion cuspateness and a correction accounting for the nonrandom organization of inclusions. Both effects increase the effectiveness that partial melt has in reducing seismic velocities.

In partially molten upper mantle containing over 1% melt, seismic wave velocity reduction per percent melt in realistically shaped melt inclusions is at least 3.6% and 7.9% for P waves and S, waves respectively. These derivatives may be smaller at melt fractions <1%, implying larger derivatives above 1%. The difference in the inferred melt fraction for these two paradigms for melt containment is the error owing to uncertainty in the geometry of melt inclusions for melt fractions other than our sample (Figure 3).

The ratio of P and S seismic wave velocities is sensitive to the effects of partial melt and relatively insensitive to the effect of subsolidus temperature changes including anelastic modulus reduction. For example, at 3% melt fraction a 1°C temperature change causes at least 3.5% change in V_P/V_S, whereas when $Q_s = 40$ at T_s, subsolidus temperature changes of 300°C are required to cause an $\sim$3% change in V_P/V_S.

References

Anderson, D.L., *Theory of the Earth*, 366 pp., Blackwell Sci., Malden, Mass., 1989.

Bai, Q., Z.-M. Jin, and H.W. Green II, Experimental investigation of the rheology of partially molten peridotite at upper mantle pressures and temperatures, in *Deformation-Enhanced Fluid Transport in the Earth's Crust and Mantle, Mineral. Soc. Ser.* vol. 8, edited by M.B. Holness, pp. 40-61, Chapman and Hall, New York, 1997.

Baker, M. B., and E.M. Stolper, Determining the composition of high-pressure mantle melts using diamond aggregates, *Geochim. Cosmochim. Acta, 58*, 2811-2827, 1994.

Cooper, R.F., and D.L. Kohlstedt, Interfacial energies in the olivine-basalt system, in *High-Pressure Research in Geophysics, Adv. Earth Planet. Sci.*, vol. 12, edited by S. Akimota and M.H. Manghnani, pp. 217-228, Cent.

for Acad. Publ. Jpn., Tokyo, 1982.

Daines, M.J., and D.L. Kohlstedt, Influence of deformation on melt topology in peridotites, *J. Geophys. Res.*, *102*, 10,257-10,271, 1997.

Dunn, R.A., and D.R. Toomey, Seismological evidence for three-dimensional melt migration beneath the East Pacific Rise, *Nature*, *388*, 259-262, 1997.

Einstein, A., Eine neue Bestimmung der Molekueldimensionen, *Ann. Phys.*, *19*, 289, 1906, (Reprinted *Ann. Phys.*, *34*, 591, 1911.

Eshelby, J.D., The determination of the elastic field of an ellipsoidal inclusion and related problems, *Proc. R. Soc. London, Ser. A, 241*, 376-396, 1957.

Faul, U.H., D. R. Toomey, and H.S. Waff, Intergranular basaltic melt is distributed in thin, elongated inclusions, *Geophys. Res. Lett.*, *21*, 29-32, 1994.

Forsyth, D.W., Geophysical constraints mantle flow and melt migration beneath mid-ocean ridges, in *Mantle Flow and Melt Generation at Mid-Ocean Ridges, Geophys. Monogr. Ser.*, vol. 71, edited by J. Phipps Morgan, D.K. Blackman, and J.M. Sinton, pp. 1-65, AGU, Washington, DC., 1992.

Hammond, W.C., and E.D. Humphreys, Upper mantle seismic wave attenuation: Effects of realistic partial melt distribution, *J. Geophys. Res.*, this issue.

Hirth, G., and D.L. Kohlstedt, Experimental constrains on the dynamics of the partially molten upper mantle: Deformation in the diffusion creep regime, *J. Geophys. Res.*, *100*, 1981-2001, 1995a.

Hirth, G., and D.L. Kohlstedt, Experimental constrains on the dynamics of the partially molten upper mantle, 2, Deformation in the dislocation creep regime, *J. Geophys. Res.*, *100*, 15,441-15,449, 1995b.

Humphreys, E.D., and K.G. Dueker, Physical state of the western U.S. upper mantle, *J. Geophys. Res.*, *99*, 9635-9650, 1994.

Isaak, D.G., High-temperature elasticity of iron-bearing olivines, *J. Geophys. Res.*, *97*, 1871-1885, 1992.

Jackson, I.M., M.S. Paterson, and J.D. FitzGerald, Seismic wave dispersion and attenuation in Åheim dunite: An experimental study, *Geophys. J. Int.*, *108*, 517-534, 1992.

Jin, Z.-M., H.W. Green II, and Y. Zhou, Melt topology in partially molten mantle peridotite during ductile deformation, *Nature*, *372*, 164-167, 1994.

Karato, S., Importance of anelasticity in the interpretation of seismic tomography, *Geophys. Res. Lett., , 20*, 1623-1626, 1993.

Karato, S., S. Zhang, M.E. Zimmerman, M.J. Daines, and D.L. Kohlstedt, Shear deformation of mantle materials: Towards structural geology of the mantle, *Pure Appl. Geophys.*, *14*, 589-603, 1998.

Kohlstedt, D.L., Structure, rheology, permeability of partially molten rocks at low melt fractions, in *Mantle Flow and Melt Generation at Mid-Ocean Ridges, Geophys. Monogr. Ser.*, vol. 71, edited by J. Phipps Morgan, D.K. Blackman, and J.M. Sinton, pp. 103-121, AGU, Washington, DC., 1992.

Kohlstedt, D.L., and M.E. Zimmerman, Rheology of partially molten mantle rocks, *Annu. Rev. Earth Planet. Sci.*, *24*, 41-62, 1996.

Mainprice, D., Modeling the anisotropic seismic-properties of partially molten rocks found at mid-ocean ridges, *Tectonophysics*, *279*, 161-179, 1997.

Mavko, G.M., Velocity and attenuation in partially molten rocks, *J. Geophys. Res.*, *85*, 5173-5189, 1980.

O'Connell, R.J., and B. Budianski, Seismic velocities in dry and saturated cracked solids, *J. Geophys. Res.*, *79*, 5412-5426, 1974.

O'Connell, R.J., and B. Budianski, Viscoelastic properties of fluid-saturated cracked solids, *J. Geophys. Res.*, *82*, 5719-5735, 1977.

Sato, H., I.S. Sacks, T. Murase, and C.M. Scarfe, Thermal structure of the low velocity zone derived from laboratory and seismic investigations, *Geophys. Res. Lett.*, *15*, 1227-1230, 1988.

Schmeling, H., Numerical models on the influence of partial melt on elastic, anelastic and electrical properties of rocks, part I, Elasticity and anelasticity, *Phys. Earth Planet. Inter.*, *41*, 34-57, 1985.

Sobolev, S.V., H. Zeyen, G. Stoll, F. Werling, R. Althern, and K. Fuchs, Upper mantle temperatures from teleseismic tomography of French Massif Central including effects of composition, mineral reactions, anharmonicity, anelasticity and partial melt. *Earth Planet. Sci. Lett.*, *139*, 147-163, 1996.

Toomey, D.R., W.S.D. Wilcock, S.C. Solomon, W.C. Hammond, and J.A. Orcutt, Mantle seismic structure beneath the MELT region of the East Pacific Rise from *P* and *S* wave tomography, *Science*, *280*, 1224-1227, 1998.

Waff, H.S., and U.H. Faul, Effects of crystalline anisotropy on fluid distribution in ultramafic partial melts, *J. Geophys. Res.*, *97*, 9003-9014, 1992.

Waff, H.S. and J.R. Bulau, Equilibrium fluid distribution in ultramafic partial melt under hydrostatic stress conditions, *J. Geophys. Res.*, *84*, 6109-6114, 1979.

Waff, H.S. and J.R. Bulau, Experimental studies of near-equilibrium textures in partially molten silicates at high pressure, in *High-Pressure Research in Geophysics, Adv. Earth Planet. Sci.*, vol. 12, edited by S. Akimota and M.H. Manghnani, pp. 229-236, Cent. for Acad. Publ. Jpn., Tokyo, 1982.

Wu, T.T., The effect of inclusion shape on the elastic moduli of a two-phase material, *Int. J. Solids Struct.*, *2*, 1-8, 1966.

Xu, Y., and D.A. Wiens, Upper mantle structure of the southwest Pacific from regional waveform inversion, *J. Geophys. Res.*, *102*, 27,439-27,451, 1997.

Zhao, D., A. Hasegawa, and S. Horiuchi, Tomographic imaging of *P* and *S* wave velocity structure beneath

northeastern Japan, *J. Geophys. Res., 97,* 19,909-19,928, 1992.

Zienkiewicz, O.C., and R.L. Taylor, *The Finite Element Method,* vol. 1, *Basic Formulation and Linear Problems,* 4th ed., 648 pp., McGraw-Hill, New York, 1989.

Zimmerman, M.E., S. Zhang, D.L. Kohlstedt, and S. Karato, Melt distribution in mantle rocks deformed in shear, *Geophys. Res. Lett., 26,* 1505-1508, 1999.

W.C. Hammond and E.D. Humphreys, Department of Geological Sciences, University of Oregon, Eugene OR 97403-1272. (bill@newberry.uoregon.edu)

Figure 1. Backscattered electron microscopic image of the melt phase from laboratory experiment by *Faul et al.* [1994]. Black represents quenched liquid melt phase; white is crystalline solid.

Figure 2. Idealized single melt inclusions illustrating the inference of three-dimensional behavior from two-dimensional melt inclusion shape data. (a) Three-dimensional oblate ellipsoid; arrows show sense of shear in the xy plane. (b) Three-dimensional cuspate inclusion with same aspect ratio. In Figures 2a and 2b the edges excited by mode II and mode III cracktip stress are shown by II and III, respectively. (c) Two-dimensional ellipse cross-sectioned cylinder. (d) Cuspate cross-sectioned cylinder. In Figures 2c and 2d shear sense arrows show mode II excited by shear in xy plane and mode III excited by shear in yz and xz planes.

Figure 3. (a) Partial melt geometries used to calculate composite material elastic properties. (b) Finite element mesh built around same geometries with elastic finite elements.

Figure 4. An enlarged example result of the finite element calculation showing the hydrostatic component of strain in the unrelaxed state. Macroscopic displacement moves top of mesh to the right, while bottom remains fixed. White outline delineates location of melt. Dark shades show compressive strains, light shades show expansive strains. The existence of stress gradients in the melt indicates that the melt is unrelaxed. Sign of the strain is a function of the inclusion orientation.

Figure 5. Two views of the three-dimensional finite element mesh used to benchmark the solution to *Mavko's* [1980] solution for the dry cuspate tubule. Dimensions of the cube are $10 \times 10 \times 10$ units, pore length is $d = 3$, pore radius is $R = 1$, $K_s = 46.7$ GPa, $\mu_s = 28.0$ GPa. Inset shows detail of mesh inside triple junction pore.

Figure 6. (a) V_P and (b) V_S seismic velocity reduction and (c) V_P/V_S as a function of temperature and partial melt content. Melt percent as a function of temperature is appropriate for water-free mantle at 30 km depth. Solid lines show results for Q that vary exponentially with temperature per *Jackson et al.* [1992]. At the solidus, T_s values of $Q_P = 90$ and $Q_S = 40$ are used. Thin vertical lines indicate melt fraction F=0%, 1%, and 2%. Circles at F=0% show where lines would cross if variable Q have values $Q_P = 45$ and $Q_S = 20$ at T_s. Crosses show where lines would cross the solidus given the assumption that Q is constant for $Q = \infty$, $Q = 100$, and $Q = 50$, as labeled in Figure 6a. The background temperature of (8) is $T_0 = 1000°$C which is $240°$C below T_s. All three crosses in Figure6c are coincident. Above the solidus the solid lines represent velocity reduction for melt containment in tubules only below 1% melt. The shaded lines represent velocity reduction for melt contained in film geometries as in Figure 3 for all melt fractions. See text for discussion and values of other constants.

Table 1. Elastic Constants Used in Calculation of Material Properties.

	Solid	Melt	
		Unrelaxed	Relaxed
K	124	40	0
μ	64	0	0

In GPa.

Table 2. Effect of Realistic Melt Geometries on Elastic Moduli and Seismic Velocity

	K	μ		$-d\ln V_P/dF$		$-d\ln V_S/dF$		$d\ln V_S/d\ln V_P$	
		Unrel.	Rel.	Unrel.	Rel.	Unrel.	Rel.	Unrel.	Rel.
Tubules	46.57	25.59	25.06	1.0	1.2	2.2	2.7	2.2	2.3
Ellipsoids	45.72	24.64	23.39	1.7	2.1	3.1	4.3	1.8	2.1
Paradigm 1: Films at All Melt Fractions									
Random cuspate	45.72	22.38	21.29	2.7	2.9	5.3	6.4	2.0	2.2
Organized cuspate	45.72	21.98	19.85	2.9	3.6	5.7	7.9	2.0	2.2
Paradigm 2: Tubules Below F=1%, Films Above F=1%									
Random Cuspate	45.72	22.38	21.29	4.5	4.8	9.0	11.0	2.0	2.3
Organized Cuspate	45.72	21.98	19.85	5.0	6.3	9.9	14.5	2.0	2.3

Elastic moduli are in GPa. Velocity reduction derivatives are in percent. Ellipsoids and films have aspect ratio $\alpha = 0.05$. Seismic velocity reduction due to tubules from *Mavko* [1980]. Velocity reduction derivatives due to ellipsoids from *Schmeling* [1985]. Bulk K and shear μ elastic moduli are for $F=2\%$. See text for definitions of relaxed (Rel.) and unrelaxed (Unrel.) elastic moduli.